Regional outer core kinematics from the time dependence of intense geomagnetic flux patches

Filipe Terra-Nova, Ingo Wardinski

Physics of the Earth and Planetary Interiors 344 (2023) 107106

Contents lists available at ScienceDirect

Physics of the Earth and Planetary Interiors

journal homepage: www.elsevier.com/locate/pepi

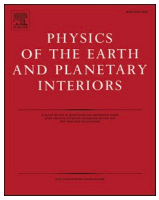

Regional outer core kinematics from the time dependence of intense geomagnetic flux patches

Filipe Terra-Nova [a,*], Ingo Wardinski [b]

[a] Laboratoire de Planétologie et Géosciences, CNRS UMR 6112, Nantes Université, Université d'Angers, Le Mans Université, 2 rue de la Houssinière, Nantes, France
[b] Institut Terre et Environnement Strasbourg, École et Observatoire des Sciences de La Terre, CNRS UMR 7063, Université de Strasbourg, Strasbourg, France

ARTICLE INFO

Keywords:
Earth magnetic field
Secular variation
Outer core kinematics
Poloidal core flow

ABSTRACT

Observations of the geomagnetic field by surface observatories and dedicated satellite missions such as the Swarm constellation provide constraints on the dynamics in Earth's outer core. In particular, global core flow models estimated by inversion of the radial magnetic induction equation provide an image of the circulation of the electrically conductive fluid at the top of the core. However, in these models the poloidal flow is much less robust than the toroidal core flow. Here, we infer regional outer core kinematics from the temporal variability of high-latitude intense geomagnetic flux patches. We develop an algorithm to fit anisotropic 2D-Gaussians to the shape of those flux patches in order to infer their area, amplitude and level of anisotropy. The temporal variabilities of these properties are used to quantify contraction, expansion, amplification, weakening and horizontal shear. Comparisons with idealized kinematic scenarios based on synthetic field and flow models allow to infer regional outer core kinematics. We found that some geomagnetic flux patches exhibit expansion and weakening corresponding to fluid upwellings, whereas other patches exhibit contraction and intensification corresponding to downwellings. In both cases the patches' area and amplitude relations follow hyperbolic curves. Our results show that the geomagnetic flux patches are affected by upwelling more often than by downwelling during the historical period. Equatorially symmetric poloidal flow prior to ≈ 1910 is inferred for the western intense patches. Kinematic scenarios where the field and flow structures centers coincide failed to reproduce the geomagnetic flux patches behavior. We recover the flux concentration efficiency of intense geomagnetic flux patches with an upwelling that resides two times its radius size away from the center of the flux patch. We also found a significant level of anisotropy over long periods for the historical geomagnetic flux patches. Anisotropic magnetic flux patches that are elongated in the direction of the shear flow may explain the east-west oriented present-day field at high latitudes of the southern Hemisphere. Overall, stretching effects at the top of the core can be deduced from our analysis of regional SV and allow further inferences on the poloidal part of the core flow.

1. Introduction

Earth's internal magnetic field provides the best image of the dynamics in Earth's deep interior. More specifically, the field morphology and its temporal variability may constrain the flow at the top of Earth's core (e.g. Holme, 2015), the way the field is maintained by a dynamo process (e.g. Olson et al., 1999) and the impact of the heterogeneous lowermost mantle on core dynamics (e.g. Gubbins et al., 2007). Core dynamics are mainly inferred from observations by inverting the geomagnetic secular variation (SV) for the fluid motion at the top of the core assuming that the magnetic diffusion is negligible (Roberts and Scott, 1965). The derivation of such motion is inherently non-unique, as one radial magnetic induction equation is solved for two unknown flow components, i.e. the toroidal and poloidal flow potentials (Backus, 1968). Therefore, some prior physical assumptions are necessary to obtain a solution. Various physical assumptions were proposed, that involve different types of poloidal and toroidal flow coupling, e.g. tangential geostrophy (LeMouël, 1984), quasi-geostrophy (Pais and Jault, 2008), helical flow (Amit and Olson, 2004) and columnar flow (Amit and Pais, 2013). For a given main toroidal flow pattern, each of these assumptions would give a different poloidal flow pattern. Furthermore, tangential geostrophy and quasi-geostrophy core flow

* Corresponding author.
E-mail address: filipe.terranova@univ-nantes.fr (F. Terra-Nova).

https://doi.org/10.1016/j.pepi.2023.107106
Received 23 May 2023; Received in revised form 31 August 2023; Accepted 18 September 2023
Available online 22 September 2023

assumptions give infinite tangential divergence if the meridional velocity is non-zero on approach to the equator, hence the upwelling and downwelling fluid motions in those models are concentrated in the equatorial region (e.g. Bloxham and Jackson, 1991; Pais and Jault, 2008; Gillet et al., 2009; Amit and Pais, 2013). Instead of coupling toroidal and poloidal flow directly, poloidal and toroidal energy spectra can be characterized by power laws derived from numerical geodynamo models and coupled by a stochastic process (e.g. Baerenzung et al., 2016, 2018; Barrois et al., 2017; Gillet et al., 2019).

Most global core flow models share similar large-scale toroidal flow features, most notably an anti-clockwise vortex below the southern Atlantic where low-latitude geomagnetic flux patches drift westward (e.g. Holme, 2015; Gillet et al., 2019). In contrast, poloidal flow structures are far less robust in global core flow models. For example, Barrois et al. (2017) resolved a large upwelling below North East Brazil around 1960 whilst Baerenzung et al. (2018) obtained strong and persistent poloidal flow structure at higher latitudes below the Indian Ocean and South Africa. Furthermore, the global ratio between toroidal and poloidal root mean square (RMS) velocity over the historical period is large, $\sim 3-10$ (Baerenzung et al., 2018), i.e. according to global core flow models the poloidal part of the flow is secondary, as it is substantially weaker than the toroidal part (Bloxham, 1992; Rau et al., 2000; Eymin and Hulot, 2005; Amit and Olson, 2006; Finlay and Amit, 2011; Amit and Pais, 2013; Barrois et al., 2017; Baerenzung et al., 2018; Gillet et al., 2019), hence its pattern is inevitably much more debatable. This provides strong motivation to identify regional geomagnetic SV produced by the poloidal flow.

If the top of the core is stably stratified, no SV due to stretching of field lines is expected (Whaler, 1980; Lesur et al., 2015). Some seismic studies (e.g. Helffrich and Kaneshima, 2010) and estimates of core thermal conductivity from mineral physics ab initio calculations (e.g. Pozzo et al., 2012) suggest that the top of the core is stably stratified (e.g. Gubbins and Davies, 2013). However, other seismic studies (e.g. Irving et al., 2018) and mineral physics experiments (e.g. Konôpková et al., 2016) suggest that stratification is not required. Lesur et al. (2015) argued that the geomagnetic SV could not be adequately explained by a purely toroidal flow, but inclusion of a weak poloidal flow is sufficient to explain the SV, suggesting that the top of the core is weakly stratified. Regional stratification may prevail if the core-mantle boundary (CMB) heat flux heterogeneity is sufficiently large (Olson et al., 2017; Mound et al., 2019). In that case, upwelling and downwelling motions may exist despite an overall stratification. Huguet et al. (2018) argued that the non-zero temporal variation of the total geomagnetic energy on the CMB is evidence for the presence of radial motions in the outer core that extend to the top of the core. Overall, the debate concerning stratification and the presence of poloidal motions below the CMB further motivates regional SV investigation.

Regional SV studies of the radial field at the CMB support the existence of westward polar vortices and associated polar upwellings (Olson and Aurnou, 1999). Chulliat et al. (2010) observed a bipolar SV structure centered at an emerging reversed flux patch at the north polar region, which they interpreted as the signature of upwelling and magnetic flux expulsion by radial diffusion. Amit (2014) interpreted persistent same-sign field and SV structures below the Southern Indian Ocean as the signature of regional downwelling.

Geomagnetic flux patches are radial field structures on the CMB. Intense flux patches are considered robust features observed in modern (Alken et al., 2021), historical (Jackson et al., 2000; Gillet et al., 2015), archeomagnetic (Constable, 2007; Jaqueto et al., 2022) and possibly even in paleomagnetic field models (Kelly and Gubbins, 1997). Here, we focus on intense patches, because these features are robust and may provide insight into elusive SV features like poloidal flow driven induction, as was done e.g. for inferring advection from intense patches in the poorly spatio-temporally resolved archeomagnetic field (Dumberry and Finlay, 2007; Amit et al., 2011).

The locations of intense high-latitude geomagnetic flux patches at the CMB may be prescribed by the inner core size and core-mantle thermal interaction. Preferred latitudinal location of high-latitude intense flux patches are related to the tangent cylinder (TC) intersection with the CMB at latitudes $\lambda_{TC} \approx \pm 69.5^{\circ}$. The solid inner core acts as a topographical fluid barrier to the rapidly rotating core flow, so that near λ_{TC} below the CMB flow convergence associated with downwellings is expected to concentrate and intensify magnetic flux patches (Christensen et al., 1998; Olson et al., 1999). In contrast, inside the TC, a thermal wind balance with polar upwelling is expected to induce flow divergence below the CMB and patches expansion and weakening (Olson and Aurnou, 1999; Cao et al., 2018; Lézin et al., 2023). In addition, seismic data shows that the lowermost mantle is laterally heterogeneous (Masters et al., 2000). Colder regions of the lowermost mantle extract more heat from the core, thus below these regions the outer core fluid is denser, prompting fluid downwellings which concentrate flux patches (Gubbins, 2003).

In order to understand regional outer core kinematics that may explain the time dependence of intense geomagnetic flux patches, here we fit 2D Gaussians to flux patches of historical and modern geomagnetic field models (Gillet et al., 2015) and of synthetic fields. We allow the Gaussian fits to be anisotropic, i.e. their north-south elongation may differ from their east-west elongation. Our 2D anisotropic Gaussian fits to intense high-latitude flux patches allow monitoring the time dependence of their amplitude, width and shape which is especially useful for identifying the elusive SV signature of the relatively weak poloidal flow as well as shear effects. We aim to study effects of stretching, therefore we focus on high-latitude patches, as theses are well identified and less mobile hence likely affected by stretching (Gubbins et al., 2007). Patches at lower latitudes are more mobile hence likely more affected by advection (Jackson, 2003).

A similar approach was taken by Amit (2014) who also inferred regional outer core kinematics from the time dependence of intense high-latitude geomagnetic flux patches. However, there are several differences between his formalism and our scheme. First, Amit (2014) fitted isotropic 2D-Gaussians, whereas we allow for anisotropy to infer the presence of shear flow. Second, he inferred persistent inductive effects by stacking SV patterns in time taking into account the patches mobility, while we rely on the time-dependent patch properties to study temporal variability. Finally, and most importantly, the scheme of Amit (2014) aimed at unraveling all induction effects, hence if advection SV is dominant it might be difficult to identify the much weaker stretching SV. In contrast, our formalism is designed to capture precisely the elusive poloidal core flow.

We explore synthetic kinematic scenarios to gain insights into the effects of upwelling, downwelling, horizontal shear flow and field-flow alignment onto flux concentration and divergence. Synthetic radial magnetic field configurations are time evolved by a large set of synthetic kinematic scenarios. In particular, we search for the kinematic scenarios that best recover the time-dependent amplitude, area and shape of intense geomagnetic flux patches. Comparison with the synthetic kinematic scenarios allow inference of the associated kinematics taking place at regions of intense high-latitude geomagnetic flux patches during the historical and modern era.

2. Methods

2.1. Morphological characterization of magnetic flux patches

For both geomagnetic field models and idealized kinematic scenarios (section 2.2), we first identify an intense magnetic flux patch by the grid location of its strongest radial field at the CMB. This is an initial localization which is later refined by the scheme detailed below. For each identified patch, we used a fixed window size in longitude and latitude around its center to fit an anisotropic 2D-Gaussian (Kac, 1939) described by:

$$B_r^P = A_{off} + A_b e^{-\left(a(\phi-\phi_b)^2+2b(\phi-\phi_b)(\theta-\theta_b)+c(\theta-\theta_b)^2\right)}, \quad (1)$$

where ϕ and θ are longitude and co-latitude, respectively, ϕ_b and θ_b are the fitted off-grid (i.e. in between grid points) patch center coordinates, A_{off} the constant background field and A_b the patch amplitude. The fitting parameters are defined as

$$\begin{aligned} a &= \frac{cos(\gamma)^2}{2\sigma_\phi^2} + \frac{sin(\gamma)^2}{2\sigma_\theta^2} \\ b &= -\frac{sin(2\gamma)}{4\sigma_\phi^2} + \frac{sin(2\gamma)}{4\sigma_\theta^2} \\ c &= \frac{sin(\gamma)^2}{2\sigma_\phi^2} + \frac{cos(\gamma)^2}{2\sigma_\theta^2} \end{aligned} \quad (2)$$

with γ the orientation of the patch anisotropy and σ_ϕ and σ_θ represent the distance over which the B_r^P peak decays from A_b to $A_b/3$ in the azimuthal and meridional direction, respectively. The time dependence of the quantities σ_ϕ, σ_θ and A_b allow inferring contraction, expansion, amplification or weakening of the patches.

We fit the regional radial magnetic field in the vicinity of the flux patch by a 2D-Gaussian (1) in a least-squares sense by searching for a least-squared minimization. Because of the truncation of core field models at spherical harmonic degree 14, the flux patches are large scale. The choice of the spatial window size weakly affects the widths σ_ϕ and σ_θ of the fitted patch, for various patch sizes. Practically, the choice of window size serves to exclude grid points of possible neighboring patches when fitting the 2D-Gaussian. We chose a fixed window grid size of 20° by 20° in longitude and latitude for all patches at all times in order to avoid introducing another parameter to our formalism. Sensitivity tests with different window sizes ranging from 15° to 30° show a weak dependence. The spatial window of the analysis is much larger than the 2° by 2° grid of the idealized kinematic scenarios (see section 3.1) and the 1° by 1° grid of the geomagnetic field models (see section 3.2). The orientation is restricted to the range $\pi/4 > \gamma > -\pi/4$ to avoid redundancy in the determination of which axis denotes the azimuthal or meridional direction.

To evaluate the level of anisotropy of the patches, we compute the ratio:

$$\xi = \frac{\sigma_\phi - \sigma_\theta}{\sigma_\phi + \sigma_\theta}. \quad (3)$$

This ratio has some desired properties. For an isotropic 2D-Gaussian $\sigma_\phi = \sigma_\theta$ hence $\xi = 0$. Positive/negative ξ values denote larger azimuthal/meridional width of the 2D-Gaussian, respectively. The Gaussian's widths σ_θ and σ_ϕ are expressed in metric units for proper calculation of ξ on a spherical surface.

For the geomagnetic field, we considered the North West, North East, South West and South East quadrants (from here after QNW, QNE, QSW and QSE, respectively) at the CMB. At each quadrant we identified the most intense normal geomagnetic flux patch center as the on-grid position of minima/maxima in the northern/southern hemisphere, respectively. In order to focus on high-latitude normal flux patches, our analysis is restricted to latitudes larger than 30°. Fig. 1 shows the radial field B_r at the CMB in 2015 and the identified intense high-latitude patches in each quadrant. Southern patches are located at higher latitudes thus their spatial windows are much smaller due to the spherical geometry.

As an example, Fig. 2 shows the intense geomagnetic flux patch center identification (red Xs) and the fitted anisotropic Gaussians (white contours) at QNE for four snapshots of the radial geomagnetic field on the CMB for the mean of the ensemble COV-OBS.x1 (Gillet et al., 2015) in 1860, 1910, 1960 and 2010. Our fit performs well, capturing several distinct patch patterns (isotropic and anisotropic) with various orientations and amplitudes as well as refined locations of centers (off-grid).

2.2. Magnetic induction by idealized field and flow

In order to understand the role of different kinematic scenarios in producing temporal changes in patches' amplitude, size and shape, we investigate synthetic radial magnetic field configurations that evolve in time by idealized core flows (synthetic kinematic scenarios). Synthetic radial magnetic fields are built from a background axial dipole field B_r^{ad} on which a pair of equatorially anti-symmetric normal flux patches is superimposed. The background field defines the polarity of the total field, though the actual dipole moment is given by the sum of the background dipole and the patches. We use an anisotropic 2D-Gaussian defined by (1) to model the radial field of a synthetic intense magnetic flux patch. For simplicity, we set the initial orientation $\gamma(0)$ at the time-step $t = 0$ to zero. The constant background field A_{off} is set to zero since B_r^{ad} is prescribed. Under those conditions, for each patch (1) simplifies to

$$B_r^P = A_b exp\left(\frac{(\phi-\phi_b)}{2\sigma_\phi^2} + \frac{(\theta-\theta_b)}{2\sigma_\theta^2}\right). \quad (4)$$

The expected ranges of initial amplitude $A_b(0)$, area $S_b(0)$ and patch

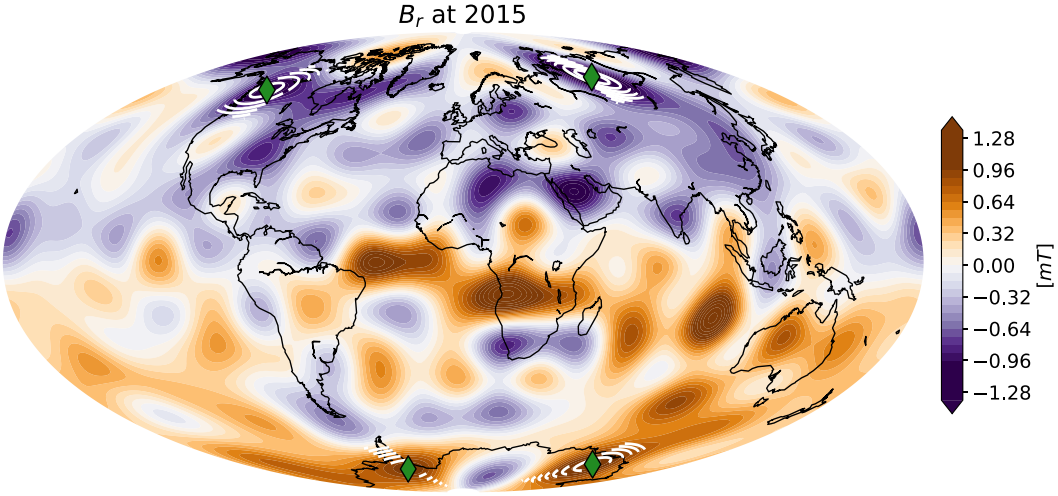

Fig. 1. Radial geomagnetic field at the CMB for a snapshot of the CHAOS7.13 model (Finlay et al., 2020) in 2015. Green diamonds are the fitted off-grid patch centers and the white contours represent the anisotropic 2D-Gaussian fits (1). (For interpretation of the references to colour in this figure legend, the reader is referred to the web version of this article.)

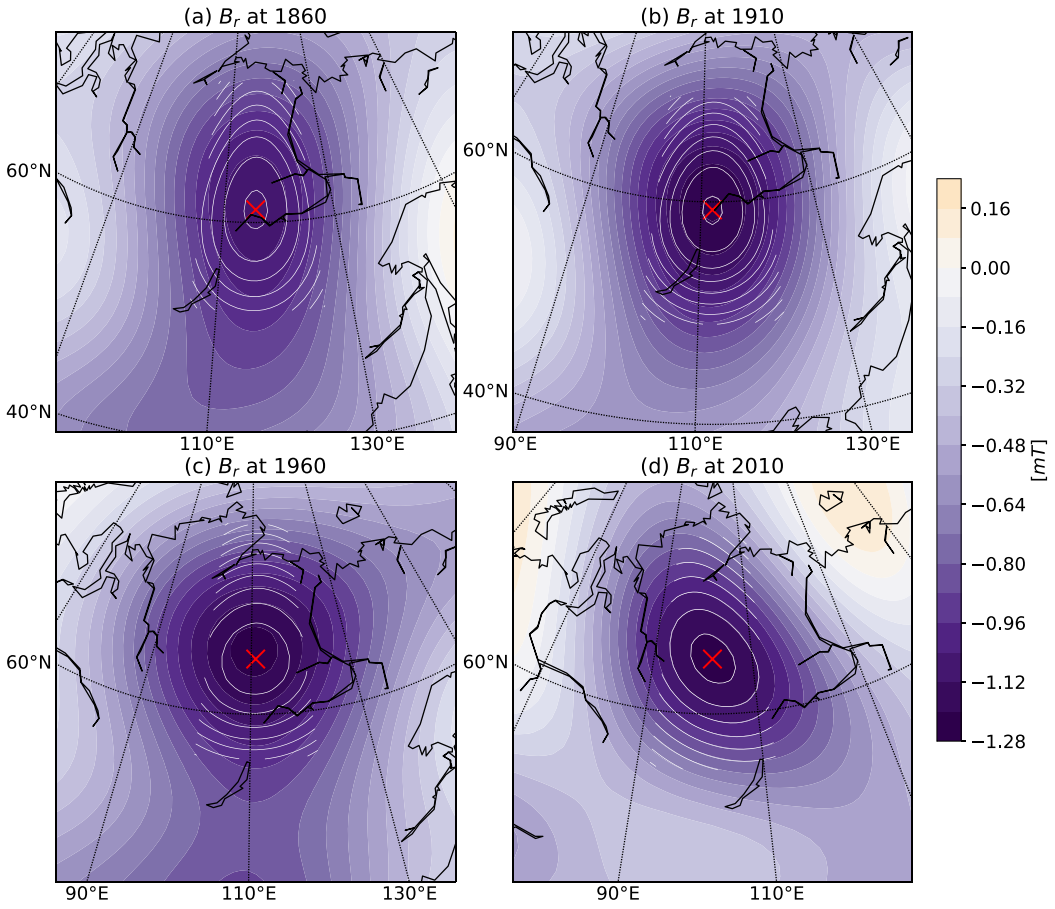

Fig. 2. Radial geomagnetic field at the CMB for four snapshots of the COV-OBSx.1 mean model (Gillet et al., 2015) at (a) 1860, (b) 1910, (c) 1960 and (d) 2010. The views are centered on the center of the intense high-latitude flux patch of the North East quadrant (below Siberia). Red crosses are the fitted off-grid patches centers and the white contours represent the anisotropic 2D-Gaussian fit (1). (For interpretation of the references to colour in this figure legend, the reader is referred to the web version of this article.)

anisotropy $\xi(0)$ are set to roughly match the patterns of the geomagnetic flux patches (see section 3.2). The global synthetic field B_r^{Syn} is given by the sum of the background axial dipole field and the Gaussian patches

$$B_r^{Syn} = B_r^{ad} + \sum_i \left(B_r^P\right)_i, \tag{5}$$

where i denotes summation over multiple patches. We set a pair of patches with opposite signs but same amplitudes and sizes, such that $\int_S B_r^{Syn} dS = 0$, where S denotes the entire CMB surface.

Next we construct kinematic scenarios to temporally evolve the radial magnetic field. Tangential core flows $\mathbf{u}_h$ just below the CMB can be represented by toroidal and poloidal potentials Ψ and Φ:

$$\mathbf{u}_h = \nabla \times \Psi \hat{r} + \nabla_h \Phi, \tag{6}$$

where $\hat{r}$ is the radial unit vector and $\nabla_h = \nabla - \partial/\partial_r$. In spherical coordinates (6) is written as:

$$\mathbf{u}_h = \frac{1}{r_c}\left(\left(\frac{1}{sin\theta}\frac{\partial \Psi}{\partial \phi} + \frac{\partial \Phi}{\partial \theta}\right)\widehat{\theta} - \left(\frac{\partial \Psi}{\partial \theta} - \frac{1}{sin\theta}\frac{\partial \Phi}{\partial \phi}\right)\widehat{\phi}\right), \tag{7}$$

where r_c is the CMB radius. We consider either a single spherical harmonic or a sum of two single spherical harmonics for our flow potentials.

The radial induction equation just below the CMB is:

$$\frac{\partial B_r}{\partial t} + \mathbf{u}_h \cdot \nabla_h B_r + B_r \nabla_h \cdot \mathbf{u}_h = \eta\left(\frac{1}{r}\frac{\partial^2}{\partial r^2}\left(r^2 B_r\right) + \nabla_h^2 B_r\right), \tag{8}$$

where η is the magnetic diffusivity. The first term of (8) is the secular variation (SV), the second represents advection by the tangential flow, the third represents stretching by the poloidal flow and the forth is magnetic diffusion. In terms of the flow potentials Ψ and Φ, (8) is written as:

$$\begin{aligned}&\frac{\partial B_r}{\partial t} + \frac{1}{r_c^2 sin\theta}\left(\frac{\partial \Psi}{\partial \phi}\frac{\partial B_r}{\partial \theta} - \frac{\partial \Psi}{\partial \theta}\frac{\partial B_r}{\partial \phi}\right) + \frac{1}{r_c^2}\left(\frac{\partial \Phi}{\partial \theta}\frac{\partial B_r}{\partial \theta} + \frac{1}{sin^2\theta}\frac{\partial \Phi}{\partial \phi}\frac{\partial B_r}{\partial \phi}\right)\\ &+B_r \nabla_h^2 \Phi - \eta\left(\frac{1}{r}\frac{\partial^2}{\partial r^2}\left(r^2 B_r\right) + \nabla_h^2 B_r\right) = 0.\end{aligned} \tag{9}$$

Typical length, velocity and magnetic diffusivity scales D, U, η, respectively, for Earth's core correspond to an advection timescale on the order of 10^2 years while the magnetic diffusion timescale is on the order of 10^5 years (e.g Holme, 2015), i.e. the magnetic Reynolds number $Rm = UD/\eta$ is ≈ 1000. Thus, the temporal evolution of the field is expected to meet the frozen-flux approximation (Roberts and Scott, 1965), i.e. strongly dominated by advection and stretching over short timescales. Following Pinheiro et al. (2019), in our kinematic scenarios that run over 50 years we neglect the radial diffusion term $\eta \frac{1}{r}\frac{\partial^2}{\partial r^2}(r^2 B_r)$. However, we keep the tangential magnetic diffusion term $\eta \nabla_h^2 B_r$ for the purpose of numerical stability. To assess the sensitivity of the results to the RMS toroidal flow magnitude a range of values corresponding to magnetic Reynolds numbers $Rm = 330 - 1000$ was explored. Then, we set the RMS poloidal flow magnitude to be lower corresponding to $Rm \approx 150$. Though, this choice turns out to be practically irrelevant since the patch intensity and area vary proportionally with the flow amplitudes.

We forward iterate (9) at the CMB. The evolution of the radial

magnetic field is time stepped using

$$B_r(t_{i+1}) = B_r(t_i) + \Delta t \frac{\partial B_r}{\partial t}(t_i). \tag{10}$$

To satisfy the Courant-Friedrichs-Lewy condition (Courant et al., 1928), which defines the necessary time step for numerical convergence based on given length and velocity scales in solutions of partial differential equations, we use a time step of $\Delta t = 1$ day (Pinheiro et al., 2019). Then, we compute the amplitude, width and anisotropy of a patch using the 2D-Gaussian fit (1). To quantify and investigate the influence of the offset between the field and the flow, we derive

$$d = \frac{\mathscr{D}(\phi_b, \theta_b; \phi_u, \theta_u)}{\sqrt{\frac{1}{2}\left(\sigma_\theta^2 + \sigma_\phi^2\right)}}, \tag{11}$$

where $\mathscr{D}$ is the spherical great distance between the center of the investigated patch (ϕ_b,θ_b) and the center of the upwelling or downwelling (ϕ_u, θ_u). This quantity is zero when the field and flow centers coincide and $d = 1$ when the center of the flow structure is at the border of the patch as defined by its Gaussian widths. We impose large-scale upwelling and downwelling flow structures using a sum of Y_2^1 and Y_2^2 spherical harmonics for the poloidal potential Φ. The combination of these two harmonics set the latitude of the upwelling/downwelling structures to 30°, hence the chosen initial latitude of the synthetic patch. This latitude was chosen to avoid limitations associated with fitting windows on the small polar caps. Although the actual intense geomagnetic flux patches appear at higher latitudes near the edge of the tangent cylinder, for our kinematic regional analysis this latitude is irrelevant. Our horizontal shear flows are built using a large-scale Y_3^0 spherical harmonic for the toroidal potential Ψ.

2.3. Inferring kinematic processes from regional SV

The action of fluid flow at the top of the core on a magnetic flux patch bounded by a null-flux radial field contour conserves magnetic flux if magnetic diffusion is negligible. More specifically, in the case of a purely poloidal flow, temporal changes in the patch area S_b and amplitude A_b are expected to obey the relation (Roberts, 2007):

$$\frac{S_b(t_i)}{S_b(t_{i+1})} = \frac{A_b(t_{i+1})}{A_b(t_i)} \tag{12}$$

where t is time, i and $i+1$ are two close snapshots. Eq. (12) implies that for any time t

$$A_b(t) = C/S_b(t) \tag{13}$$

where C is a constant that represents the magnetic flux enclosed by a patch.

In practice it is impossible to bound an intense magnetic flux patch of normal polarity by a $B_r = 0$ contour. We thus assigned a patch area S_b as the ellipse area defined by the two widths of the Gaussian fit (1):

$$S_b = \pi \sigma_\phi \sigma_\theta. \tag{14}$$

Here at each t the patch ellipsoidal meridional and azimuthal axes are enclosed by contours of $A_b(t)/3$. In order to obtain a measure of amplitude independent of the area inference, we simply assigned the amplitude of the Gaussian fit (1) as the patch amplitude A_b. We will show that indeed with upwelling and downwelling (13) holds qualitatively, i.e. the amplitude of a patch $A_b(t)$ evolves inversely to its surface $S_b(t)$. However, when applied to our regional characterization, quantitatively (13) is not optimal. We therefore generalized (13) to

$$A_b(t) = C/S_b^\alpha(t) \tag{15}$$

thus a hyperbolic fit between A_b and S_b may provide evidence for regional stretching SV. In (15) the power α denotes the time dependence of flux concentration (or dispersion) efficiency. We emphasize that the reason for this generalization is that in our scheme we do not consider null-flux contours of B_r at the CMB, because normal flux patches are not enclosed by null-flux contours. Instead, we consider the 2D-Gaussian fit to the patches. The product between S_b and A_b is therefore not the total flux, but a proxy of it. Moreover, while under a frozen-flux scenario stretching effects for a region enclosed by a null-flux contour correspond to $\alpha = 1$, in our characterization, in which the product of A_b and S_b is not perfectly conserved, α may deviate from unity.

In contrast, if magnetic flux is expelled from the deep core to the CMB (Bloxham, 1986; Terra-Nova and Amit, 2020; Troyano et al., 2020), the patch may increase both in amplitude and area, suggestive of a relation such as

$$\frac{S_b(t_i)}{A_b(t_i)} \approx \frac{S_b(t_{i+1})}{A_b(t_{i+1})}. \tag{16}$$

From (16) it implies that for any time t, $A_b(t) \approx DS_b(t)$ where D is a positive constant. Thus a linear fit with a positive slope between A_b and S_b may provide evidence for diffusive SV. We examine these fits to each patch separately.

The action of toroidal horizontal shear flow on a patch is not expected to affect its size and amplitude, but it is expected to produce anisotropy. We therefore explore the evolution of ξ as defined by (3) in kinematic scenarios with a toroidal shear flow. In particular we examine the dependence of the anisotropy on the magnitude of the shear flow.

3. Results

3.1. Idealized kinematic scenarios

Fig. 3 shows two scenarios of patch evolution due to downwelling and horizontal shear flow, respectively. The left column of Fig. 3 displays the initial conditions of isotropic patches ($\xi = 0.0$ (3)). In the case of downwelling the patch and flow centers coincide, i.e. $d = 0$ (11). The right column of Fig. 3 shows the configuration after 50 years. In the downwelling scenario (Fig. 3 top), after 50 years (Fig. 3 top right), the patch is reaching stronger amplitude values (darker colour) and is confined to a smaller area (smaller white ellipse). In the shear scenario (Fig. 3 bottom) the patch exhibits significant increase in anisotropy (see circles becoming ellipses).

3.1.1. Downwelling and upwelling

We evaluate the dependence of the relation between patch amplitude A_b and area S_b on the initial values $A_b(0)$ and $S_b(0)$ for $d = 0$ by exploring a range of initial values of A_b and S_b. Fig. 4 shows that all patches either intensify and contract (by downwelling) or weaken and expand (by upwelling). Therefore, the hyperbolic fits to (15) are excellent ($R^2 \approx 1.000$). The measure of the time dependence of the flux concentration (or dispersion) efficiency α in (15) increases/decreases for increasing/decreasing $A_b(0)$ and decreasing/increasing $S_b(0)$, respectively.

Fig. 4 also shows that westward drift produces very small temporal changes in S_b and A_b values as the points cluster (see black symbols). This scenario also confirms that the technical/numerical role of tangential magnetic diffusion in our approach indeed performs well without significantly affecting the resulting SV.

Next, we consider the influence of field-flow interaction on the time dependence of flux concentration efficiency α (15) by monitoring the initial offset between the field and the flow structure d (11). Fig. 5 shows the results for several values of d with an initial isotropic patch under the influence of downwelling (a, c) and upwelling (b, d), respectively. We fix the initial values of the patch amplitude $A_b(0)$ and area $S_b(0)$ for all cases. We apply changes in d in the azimuthal direction to avoid amplitudes changes related to the axial dipole background field. Figs. 5a

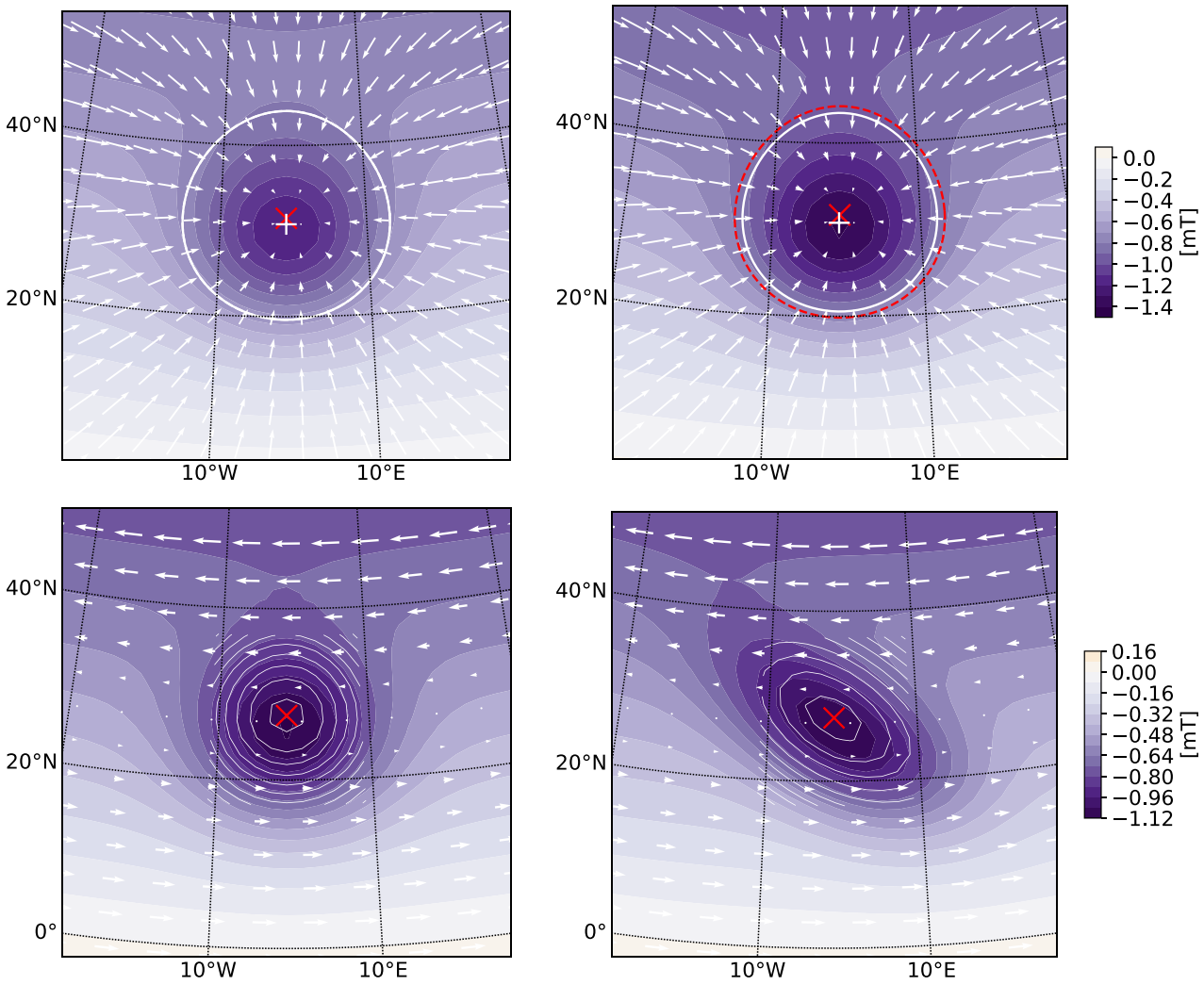

Fig. 3. Left: Initial synthetic fields (colour maps) and idealized flow scenarios (arrows). Right: The resulting synthetic field after 50 years of time evolution. Red Xs denote the identified flux patch centers (ϕ_b,θ_b). Top: Downwelling without initial field-flow offset. White crosses denote the centers of poloidal flow structures (ϕ_u,θ_u) and single white ellipses denote patch area S_b defined by its Gaussian widths. Dashed red line on the right panel denotes the initial $S_b(0)$ for comparison with the final state (solid white ellipse). Bottom: Horizontal shear flow. White enclosed contours represent several isolines of the anisotropic 2D Gaussian fit obtained from (1). Initial/Final values are $A_b = 1.16/1.37\ mT$ and $S_b = 1.70/1.47 \times 10^6$ km^2 for the downwelling scenario and $\xi = 0.00/0.26$ for the shear flow scenario, respectively. (For interpretation of the references to colour in this figure legend, the reader is referred to the web version of this article.)

and b show again that downwelling causes patch intensification and contraction while upwelling leads to weakening and expansion (see temporal evolution indicated by arrows). The hyperbolic fit parameter α strongly depends on d (Figs. 5c and d). When patches are further from the center of the downwelling structure, the time dependence of the flux concentration efficiency increases (Fig. 5c) because the patch approaches rapidly the center of the flow structure. We repeat this for a patch under the influence of upwelling (Fig. 5b). In contrast to the downwelling scenario, for upwelling with increasing d the time dependence of flux concentration efficiency α decreases (Fig. 5d) because in this case the patch migrates rapidly away from the center of the flow structure.

Poloidal flow produces both stretching and advective SV, the latter increases with larger distances (i.e. offsets) between the field and flow centers. Thus for downwelling with large d the patch approaches rapidly the center of the flow structure, so the concentration of flux efficiency increases rapidly and α is much larger than for small d. In contrast for upwelling with large d the patch rapidly moves away from the flow center, therefore the concentration of flux efficiency decreases rapidly and α becomes much smaller than for small d.

The goodness of the fit R^2 (also given in Fig. 5) shows that the dependence of results on d is similar for upwelling/downwelling: in both cases the results deviate from the fits at later times and for larger d (Figs. 5a and b). The hyperbolic fit is expected to be optimal for pure stretching ($d \approx 0$) so the deviations from fits for larger d are due to the mixed effect of stretching and advection by the poloidal flow. Nevertheless, in all cases the R^2 values are close to unity.

Figs. 5c and d also show for downwelling and upwelling, respectively, the dependence of the total variation of the level of anisotropy $\Delta\xi = \xi(50) - \xi(0)$ on d. The values of ξ are small for all patches at all times, less than 2.5% difference between σ_ϕ and σ_θ. Nevertheless, the total temporal change of these small anisotropy values $\Delta\xi$ exhibits an interesting dependence on d. Since d is applied only in the azimuthal direction (towards the east), the stretching is more effective in this direction, i.e. $|\partial u_\phi/\partial\phi| > |\partial u_\theta/\partial\theta|$. For downwelling $\partial u_\phi/\partial\phi < 0$, promoting meridional stretching which yields positive ξ (Fig. 5c), whereas for upwelling $\partial u_\phi/\partial\phi > 0$, giving meridional contraction of the patch anisotropy which results in negative ξ (Fig. 5d).

3.1.2. Horizontal shear flow

Finally, we explore the horizontal shear flow scenario and its dependence on the flow magnitude. Fig. 6 shows the time dependence of

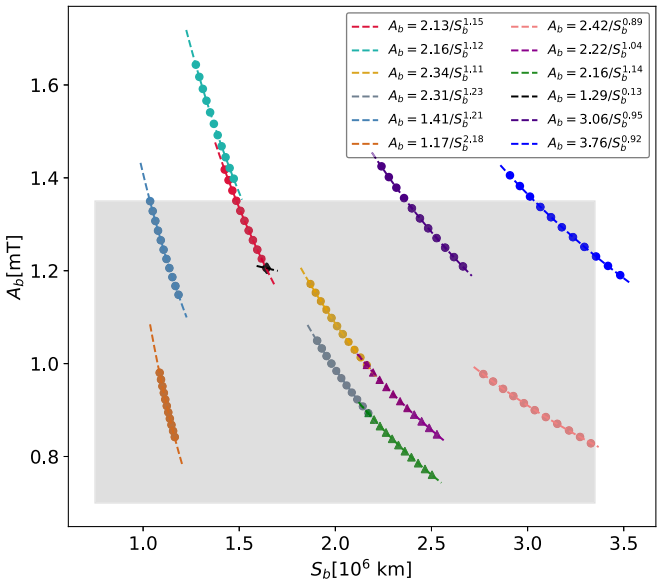

Fig. 4. The relation between patches' amplitude and area for $d \approx 0$ and $\xi(0) \approx 0$. Circles, triangles and diamonds denote downwelling, upwelling and westward drift, respectively. Note that the black diamonds cluster thus they are difficult to visualize. Light gray rectangle corresponds to the range of values for geomagnetic high-latitude normal flux patches (see section 3.2). Dashed lines are the hyperbolic fits to (15). The temporal evolution is towards up/left for downwellings and towards down/right for upwellings. The values of R^2 that quantify the goodness of fits were ≈ 1.0 for all patches under downwelling or upwelling influence. Results are plotted in 5-years intervals.

the flux patches anisotropy ξ (3) for variable *Rm*. Note that the *Rm* range is conservative because while the global estimate for Earth's core is $Rm \approx 1000$, locally the flow magnitude may be much higher (Finlay and Amit, 2011). We find that the stronger the flow magnitude the faster the increase in patch anisotropy. Furthermore, Fig. 6 indicates that the patch anisotropy accelerates, especially at the early stages when the patch is isotropic.

3.2. Geomagnetic flux patches

We now present results obtained by applying the formalism to the historical geomagnetic field model COV-OBSx.1 (Gillet et al., 2015) during the period 1840–2010 every 5 years to characterize high-latitude intense flux patches of the radial field at the CMB. We set a spatial resolution of 1° by 1° in longitude and latitude. Fig. 7 shows the time-dependence of the longitude and latitude of the identified centers (ϕ_b,θ_b) of the most intense high-latitude normal flux patches for each quadrant (see section 2.1) obtained from the 2D-Gaussian fit (1). Discontinuities in the tracking occur when a new patch becomes the most intense. Only in the QNE a single persistent patch is identified as the most intense for the entire studied period, while one discontinuity is found in each of the other three quadrants during the historical era.

Fig. 7a shows that the longitudinal positions of the intense flux patches are close to the maxima of the longitudinal average of lower-most mantle seismic shear wave anomalies (Masters et al., 2000), particularly the eastern patches. Generally, most patches have been drifting westward (see negative slopes in Fig. 7a), but the QSE patch drifted eastward in recent times and the QSW patch showed intermittent westward/eastward drifts between 1900 and 1975. Fig. 7b shows that all patches reside near the edge of the tangent cylinder though the southern patches are somewhat closer to the tangent cylinder edges than the northern patches. The patches meridional drifts are less pronounced, especially after 1965 (Fig. 7b). Between 1915 and 1965, the QNE patch showed some northward drift. Before 1915, weak northern/southern drifts are observed for the QSE/QSW patches, respectively, while the northern patches exhibit opposite corresponding meridional drifts.

Fig. 8 shows the azimuthal and meridional patches widths (σ_ϕ and σ_θ, respectively) as functions of time for the historical period as well as the temporal evolution of their amplitudes. Prior to 1900, σ_θ was larger than σ_ϕ in all quadrants. Between 1900 and 1925, the azimuthal direction became the larger axis of the Gaussian fit in QNW, QSW and QSE as new patches appeared in these quadrants. For QNW and QSE this new anisotropy persists until present. In QSW an isotropic patch existed for some time, then its σ_ϕ value became much larger than σ_θ on approach to present. Overall, Fig. 8 indicates an inverse relation between the amplitude A_b and the meridional width σ_θ. This inverse relation is most apparent for the QNE patch, which has also the largest amplitude, while QSE has the lowest. The patches' amplitudes in QNW, QSE, QSW decreased fast in the early years studied. The QNW patch continued to weaken but much slower after 1910, the QSW patch exhibited little variability after 1900, and the QSE, which was the weakest until 1915, became stronger than the QNW and QSW patches. Finally, the average orientation of patch anisotropy γ (2) for all patches and all times is below 10° (not shown).

Fig. 9 shows the relation between the amplitude and the area of the identified geomagnetic flux patches. Considering absolute amplitudes, decreasing hyperbolic fits suggestive of SV due to stretching are found for six of the seven identified patches. An increasing linear fit that suggests SV due to diffusive processes is found only for the younger patch in the QNW. Note however that the fit for this patch is very poor ($R^2 \approx 0.272$). Of those suggestive of stretching effects, the western patches show an area increase and amplitude decrease with time which implies upwellings. The time dependence trends are more complex for the Eastern patches. In the QSE, the older patch expands and weakens in time suggestive of upwelling, while the younger patch contracts and strengthens in time which implies downwelling. The patch in QNE exhibits intermittent downwelling and upwelling SV with the former being more prominent.

The time dependence of flux concentration (or dispersion) efficiency α differs significantly among the six hyperbolic fits (Fig. 9). The lowest $\alpha = 0.06$ value is found for the younger QSW patch (dashed line in Fig. 9c), whereas the largest $\alpha \approx 0.6$ values are found for the old QNW, QSW and QSE patches (solid lines in Fig. 9a, b and d). This variability in α values may indicate different kinematic processes acting in different CMB regions.

The time dependence of the levels of anisotropy of the identified high-latitude intense geomagnetic flux patches are shown in Fig. 10. Generally, patches exhibit larger meridional width ($\xi < 0$) before 1900 and larger azimuthal width ($\xi > 0$) after 1925. Large negative values of $\xi < -0.2$ were found for all patches, with the lowest being registered at QSE. Large positive values of $\xi > 0.2$ were only registered for the western patches. Remarkably, the QSW patch from 1930 until present changed from an isotropic pattern to the largest anisotropy level reaching $\xi \approx 0.5$.

Finally, we apply the formalism to the high-quality and resolution modern internal geomagnetic field model CHAOS7.13 (Finlay et al., 2020), based on satellite measurements such as the Swarm constellation (Friis-Christensen et al., 2006), during the period 1997–2020 in 1 year interval with a spatial resolution of 1° by 1° in longitude and latitude. Fig. 11 shows the relation between the amplitude and the area of the identified patches. Decreasing hyperbolic fits suggestive of stretching SV are found for four of the five identified patches, though in the more recent QNW patch the amplitude changes are very small (see flat curve in Fig. 11a). The southern Hemisphere patches show contraction and intensification suggestive of downwelling signatures (Fig. 11c and d). An increasing linear fit suggestive of diffusive SV is found for the older QNW patch (Fig. 11a). The QNE patch exhibits a transition from inferred downwelling to upwelling (Fig. 11b), highlighting the intermittency of stretching SV that is also seen in the historical era for the same patch (Fig. 9b).

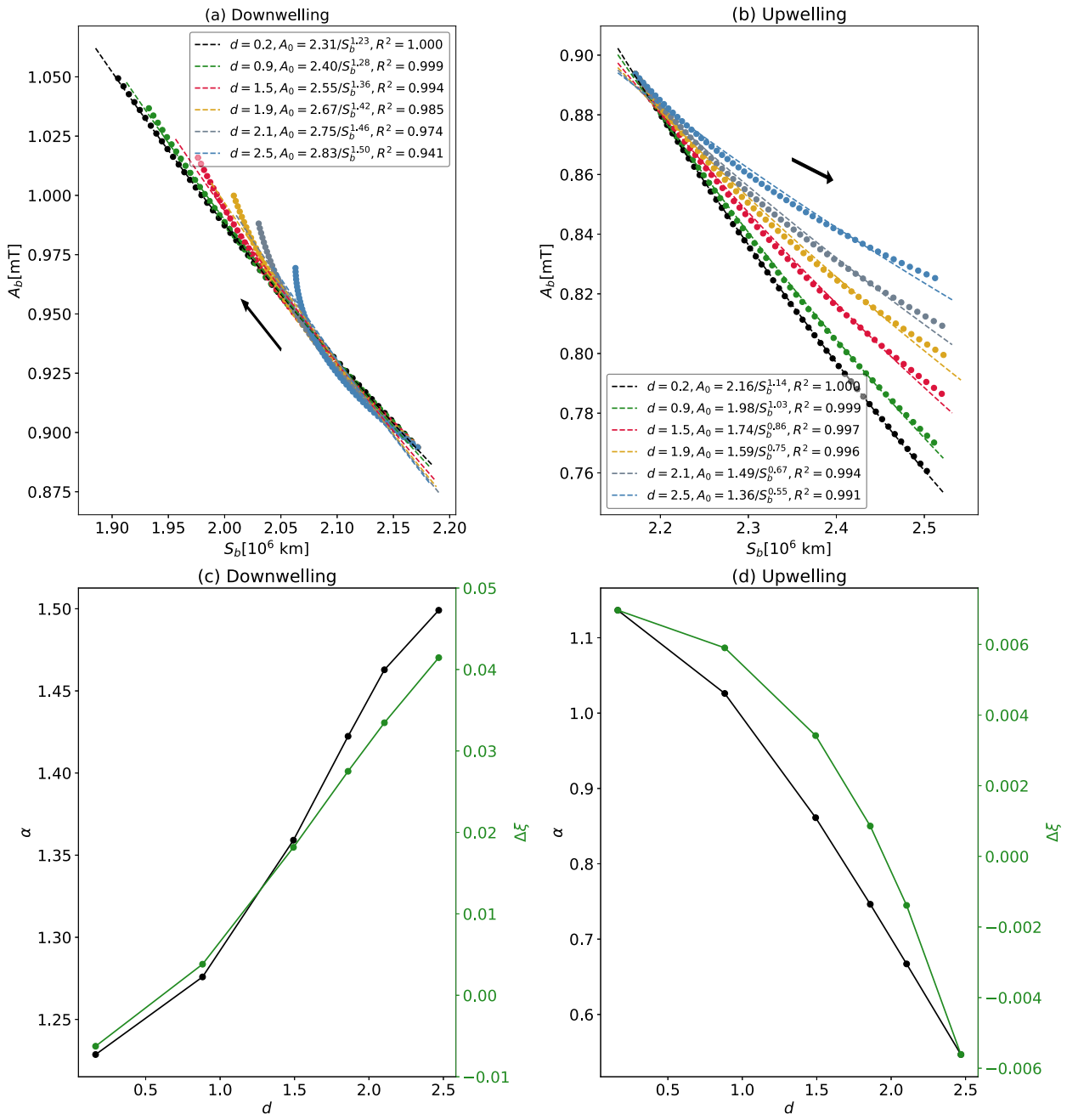

Fig. 5. Patch amplitude vs. area (a, b) for idealized kinematic scenarios under downwelling (a) and upwelling (b). The dashed lines are hyperbolic fits to (15), the arrows denote the sense of time evolution. (c, d) Time dependence of flux concentration efficiency α and the total change in patch anisotropy $\Delta\xi$ vs. the initial distance between field and flow structures d for downwelling and upwelling, respectively.

We also monitored the level of anisotropy of the identified high-latitude intense flux patches for the modern field (Finlay et al., 2020). The ratio ξ (3) in Fig. 12 prolongs the results in Fig. 10 for each quadrant. The QSW patch still has the largest anisotropy, $\xi \approx 0.4$. However, during the past 20 years ξ is not increasing as in the historical era model, but it remains constant.

4. Discussion

Latitudes of intense normal flux patches are thought to be caused by downwellings at the intersection of the TC with the CMB, θ_{TC}. We only identify one patch center inside the TC, in QSW from 1905 until present (Fig. 7b). This patch shows weak upwelling effects (Fig. 9c). Other patches, which reside just outside the TC are not exclusively dominated by downwelling, though the closest patch to θ_{TC}, the younger patch in QSE (Fig. 7b), mainly exhibits downwelling effects (Fig. 9d). Some patches may exhibit upwelling signatures, but this may not be necessarily indicative of their entire history. These patches could indeed be formed and maintained by downwellings long before the historical era when they were identified as most intense features. Thereafter, the flow may vary and patches may become subject to other flow features (e.g. upwellings).

The longitudes at which intense geomagnetic flux patches appear may be determined by CMB heat flux heterogeneities (Gubbins et al., 2007). Indeed our results show that locations of flux patches are well correlated with positive lower mantle seismic shear wave velocity anomalies, especially the eastern patches that reside in one of these two branches of preferred longitudes throughout the entire period.

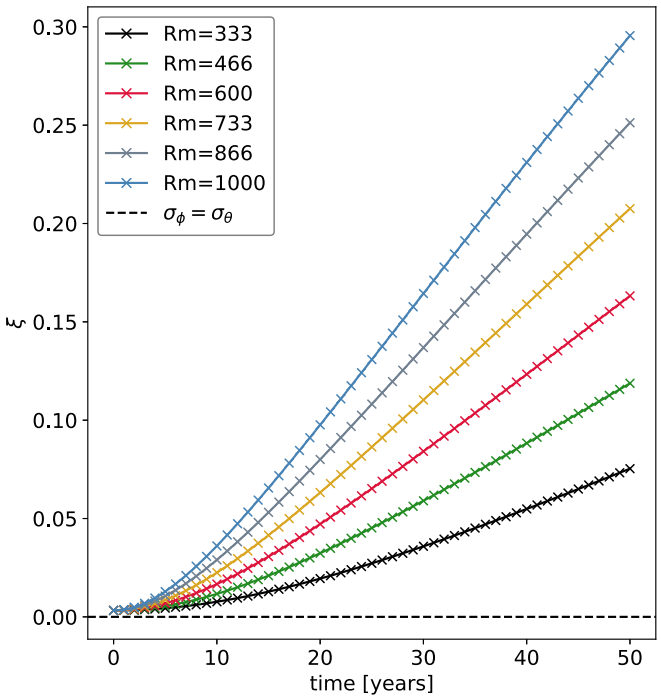

Fig. 6. The time dependence of the anisotropy ξ (3) of idealized flux patches under the influence of shear flow. The dashed line represents perfect isotropy.

Remarkably, these eastern patches are also the ones that show SV features related to downwelling (contraction and intensification of flux) during the historical period. This may indicate that the boundary effect may apply in a statistical sense, and that patches are not locked, but rather appear more often at preferred sites than elsewhere (Olson and Christensen, 2002; Amit et al., 2010; Terra-Nova et al., 2019). Therefore, the western patches may also be mantle controlled, with their historical locations representing the chaotic nature of the geodynamo which yields strongly time-dependent longitudinal positions of flux patches around their preferred sites prescribed by the heterogeneous CMB heat flux.

The temporal evolution of geomagnetic flux patches' amplitude A_b and area S_b are monitored by the 2D-Gaussian fits (Fig. 9). The A_b vs. S_b relations follow hyperbolic curves, as expected (Roberts, 2007). To refine the characterization of the A_b vs. S_b curves we generalize the quantitative description of flux concentration by adding the power parameter α (15) which we interpret as the temporal variability of the flux concentration efficiency. The two hyperbolic curves with the highest fit quality give comparable $\alpha \approx 0.6$ for early western geomagnetic flux patches (Figs. 9a and c). This may indicate equatorially symmetric poloidal flow prior to 1910. Some patches exhibit alternating upwelling and downwelling, e.g. the QNE patch which shows episodes of expansion and weakening as well as episodes of contraction and intensification (Fig. 9b). This suggests that the related high-latitude poloidal flow varies on relatively short timescales and, perhaps, alternates direction. We also observe contraction and weakening of the recent QNW patch area and its amplitude, respectively (Fig. 9a), which may be due to the action of radial diffusion.

The level of field/flow alignment strongly affects the temporal variability of the flux concentration efficiency. A large distance between a downwelling and a flux patch leads to a patch rapidly approaching the downwelling hence promoting increasing flux concentration efficiency α. Conversely, a large offset between an upwelling and a patch gives decreasing α values. Indeed, we obtained a much larger range of α values by changing d than for variable initial A_b and S_b. In particular, we recover the α values of intense geomagnetic flux patches with an upwelling that resides two times its radius size away from the center of the

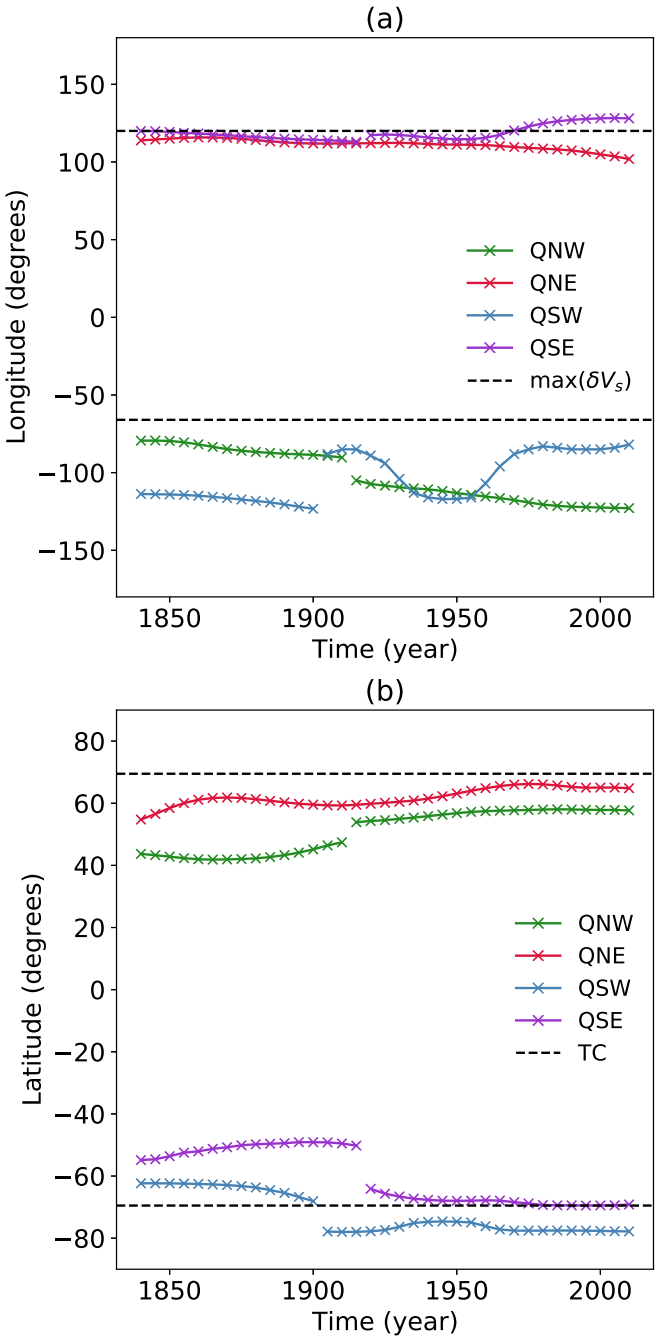

Fig. 7. The time dependence of the longitude (a) and latitude (b) of the identified centers (ϕ_b, $90^\circ - \theta_b$) obtained by the Gaussian fit. In (a) dashed lines correspond to the maxima of the longitudinal average of the lowermost mantle seismic shear wave velocity anomalies (Gubbins, 2003) from the tomographic model of Masters et al. (2000). In (b) dashed lines correspond to the latitudes of the intersection of the inner core tangent cylinder and the CMB.

magnetic flux patch (Fig. 5b). In contrast, with downwelling increasing d gives increasing α, hence we fail to reproduce the geomagnetic α values with off-phase downwelling (Fig. 5a).

A significant level of anisotropy $|\xi| > 0.2$ is found over long periods for the historical geomagnetic flux patches (see Fig. 10). The recent QSW patch showed weak temporal changes in amplitude but significant changes in area size (Fig. 9c) and anisotropy (Fig. 10), possibly indicating the action of horizontal shear flow in this region. Strong shear flows produce anisotropy with a strong dependence on the flow magnitude. The action of shear flow leads to elongated magnetic flux in

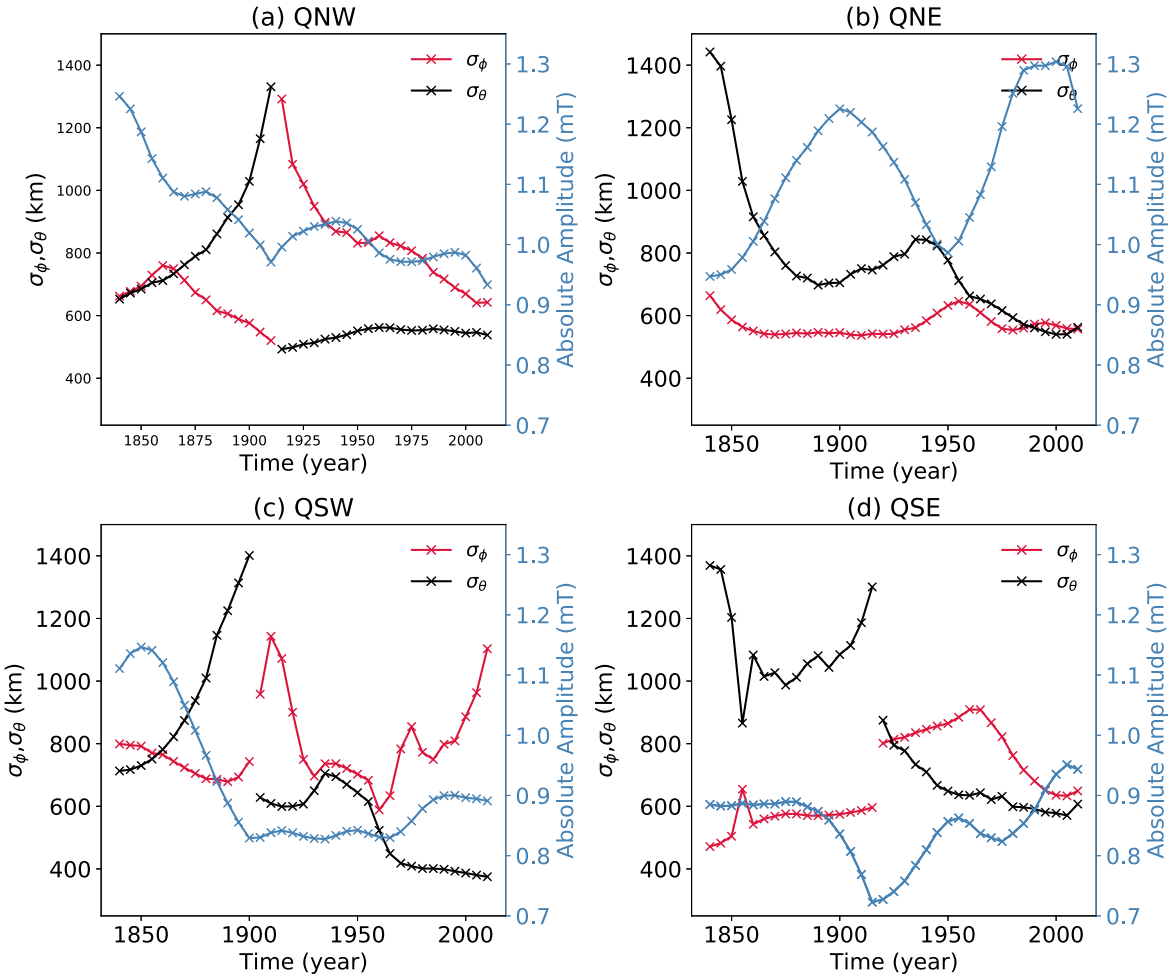

Fig. 8. The time dependence of the patches azimuthal (red) and meridional (black) widths (σ_ϕ and σ_θ, respectively) of intense geomagnetic flux patches and their absolute amplitudes (blue). Each subplot represent a patch of a quadrant, i.e. North West, North East, South West and South East. (For interpretation of the references to colour in this figure legend, the reader is referred to the web version of this article.)

the direction of the shear. This mechanism may explain the east-west oriented present-day field at high latitudes of the southern Hemisphere (Livermore et al., 2017). The anisotropy change of $\Delta\xi \approx 0.46$ that developed in QSW during the past ≈ 80 years (Fig. 10) corresponds to a rate of $\Delta\xi/\Delta t \approx 0.006\ \mathrm{yr}^{-1}$. Based on the modern field in QNE we found a rate of $\Delta\xi/\Delta t \approx -0.007\ \mathrm{yr}^{-1}$ (Fig. 12). Our synthetic shear flow scenarios produce $\Delta\xi \approx 0.3$ in 50 years for $Rm \approx 1000$ (Fig. 6), i.e. we recover $\Delta\xi/\Delta t \approx 0.006\ \mathrm{yr}^{-1}$. Note that this Rm value corresponds to the global core flow estimate, while regional values can reach much higher values (Finlay and Amit, 2011). Therefore, shear flow may easily explain the observed rate of anisotropy.

Applied to the modern field built from high-quality and high-resolution satellite data, the main results of our formalism are in qualitative agreement with the results from the historical era. However, there are some important differences. We found smaller S_b values in CHAOS7.13, possibly due to the higher resolution of this model. Some differences in ξ are also observed, e.g. in the QSW ξ increases in COV-OBS.x1 but remains constant in CHAOS7.13 over the past 20 years.

It is important to note that the geomagnetic field models have some uncertainties. This is especially the case in the southern hemisphere at early epochs due to fewer magnetic observatories hence larger gaps in spatial coverage as well as large uncertainties at some observatories (e.g. Jackson et al., 2000; Matzka et al., 2010; Gillet et al., 2015). Such uncertainties might bias our results for the earlier epochs. For example, the discontinuities in the identified patches in 1910–1920 may be related to a peak in the amount of data at that period (Jonkers et al., 2003; Matzka et al., 2010). Overall, any conclusions concerning the earlier epochs should be taken with caution.

Several effects not explored in this study may affect the idealized kinematic scenarios results. First, we focused on results with steady flows. We also examined a time-dependent downwelling oscillatory amplitude $A_u(t) = A_u(0)\left(1 + \frac{1}{4}cos(\omega t)\right)$ with frequencies $\omega = 2\pi/5\ \mathrm{yr}^{-1}$ and $\omega = 2\pi/50\ \mathrm{yr}^{-1}$ (Pinheiro et al., 2019). The results are similar (not shown). Second, we fixed $Rm = 1000$. However, larger/smaller Rm would increase/decrease both A_b and S_b proportionally, hence α is not affected by the flow amplitude. Third, radial diffusion was not explored by the kinematic scenarios because it is not feasible within a 2D framework (Metman et al., 2018). These non-modeled features could explain the failure of our approach to reproduce $\alpha < 0.89$ for synthetic downwellings, while contracting/intensifying geomagnetic flux patches have $0.31 < \alpha < 0.36$. Alternatively, the moderate values of α for the geomagnetic flux patches compared to those obtained in our idealized kinematic scenarios may indicate weak stratification at the top of the core (Lesur et al., 2015). Clearly, the spatio-temporal complexity of the kinematic scenarios affects the results. Nevertheless, we demonstrate that simple kinematic scenarios may recover several key aspects of regional SV.

5. Conclusions

In this paper, we proposed a formalism to infer regional core kinematics, in particular regional poloidal flows, which are otherwise diffi-

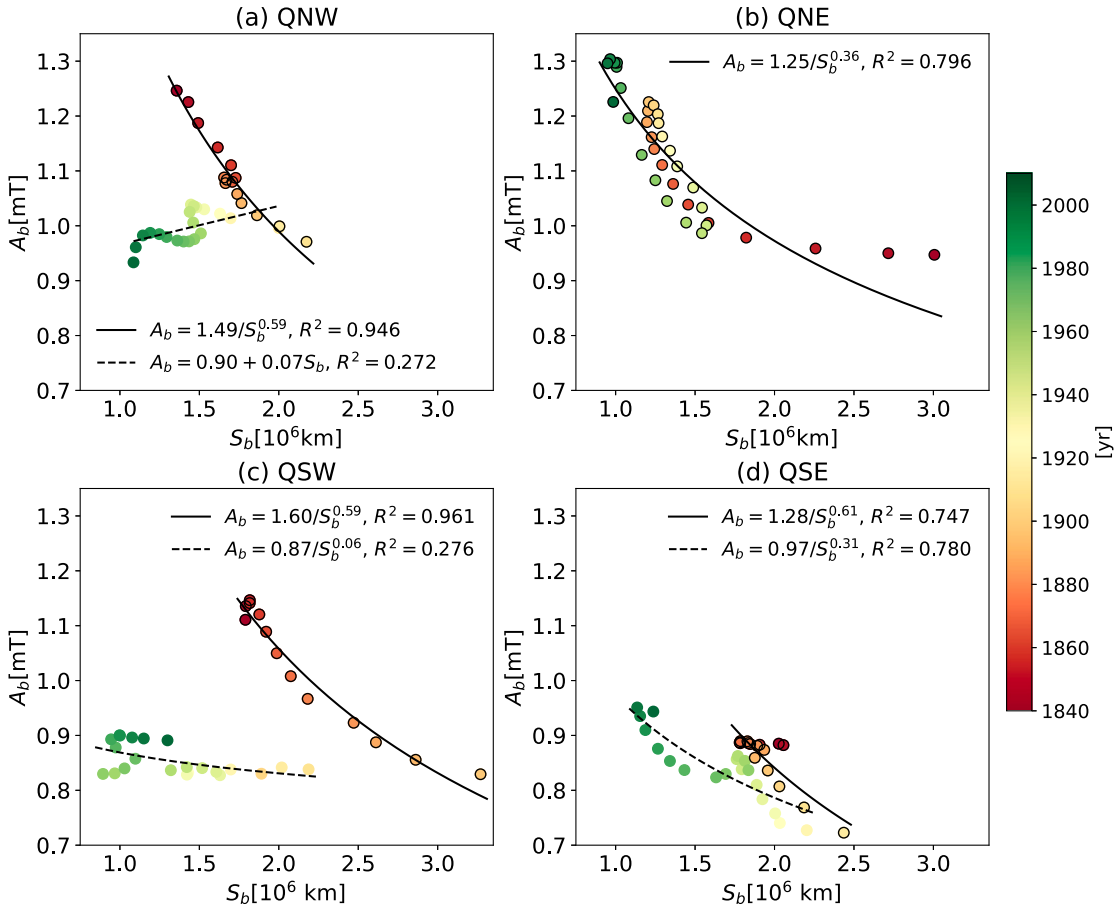

Fig. 9. Patches amplitude A_b vs. area S_b (14) for each identified high-latitude intense geomagnetic flux patch. Fits are denoted by black lines. All fits are hyperbolic except for the dashed line in (a) (see legends). Colors denote time (see colorbar). The goodness of fits are measured by R^2.

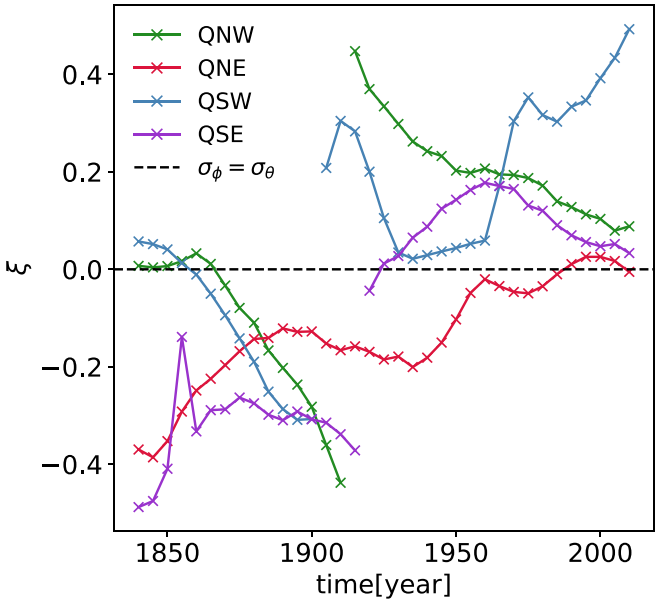

Fig. 10. The time dependence of geomagnetic flux patches anisotropy ξ (3). The dashed line represents perfect isotropy. Positive/negative ξ values correspond to a patch elongated in the azimuthal/meridional direction, respectively.

cult to robustly infer in global core flow inversions. We applied a 2D-Gaussian fit to intense geomagnetic flux patches over the historical era and to synthetic patches that were evolved by idealized kinematic scenarios. The temporal evolution of patches' amplitude, area and shape were monitored in order to quantify contraction, expansion, amplification, weakening or horizontal shear of the patches. We compared the results obtained from geomagnetic flux patches and idealized kinematic scenarios in order to determine regional kinematics at the top of the core. In particular, we inferred the stretching effects related to poloidal flow acting on intense geomagnetic flux patches to deduce the flux concentration (or contraction) efficiency α during the historical period. In addition, we determined the amplitude of shear flow that may account for anisotropy changes $\Delta\xi$ of the geomagnetic flux patches.

We gained fundamental insights into core kinematics by studying idealized kinematic scenarios, in particular their hyperbolic fits to the A_b vs. S_b dependency. Reproducing low geomagnetic-like $\alpha < 0.6$ values with $d = 0$ requires unrealistic small values of initial patch amplitude or unrealistic large values of initial patch area. This led us to conclude that on-phase configuration of field and upwelling/downwelling structures cannot reproduce the α values observed for geomagnetic flux patches.

In core flow models obtained from global SV inversions, the poloidal flow is not well constrained, for several reasons. First, the dominant toroidal flow (Finlay and Amit, 2011) masks the SV induced by the poloidal flow. Second, the poloidal flow is related to the dominant toroidal flow via different physical assumptions (e.g Holme, 2015). Finally, global core flow inversions are regularized. Regional studies may provide valuable insights as has been applied to intense flux patches in archeomagnetic field models (e.g. Dumberry and Finlay, 2007; Amit et al., 2011; Terra-Nova et al., 2015). Here we proposed an innovative

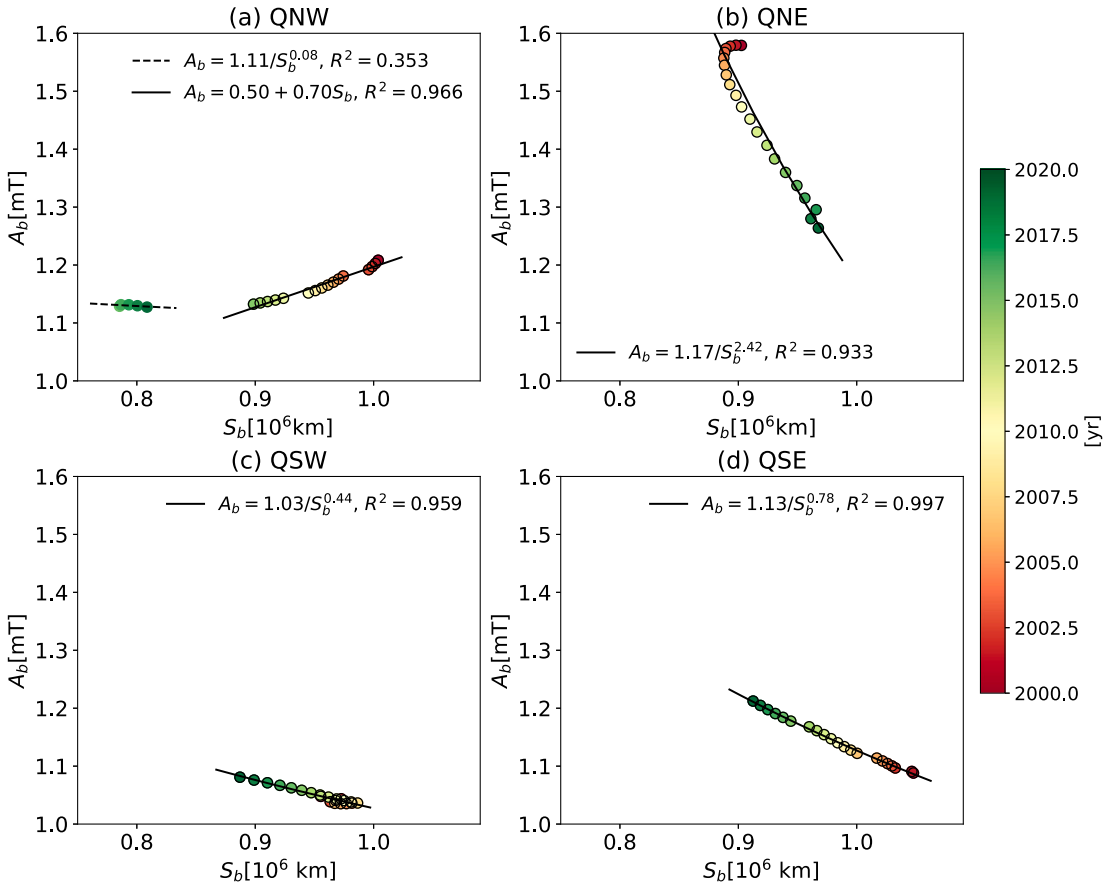

Fig. 11. As in Fig. 9 for the CHAOS7.13 geomagnetic field model.

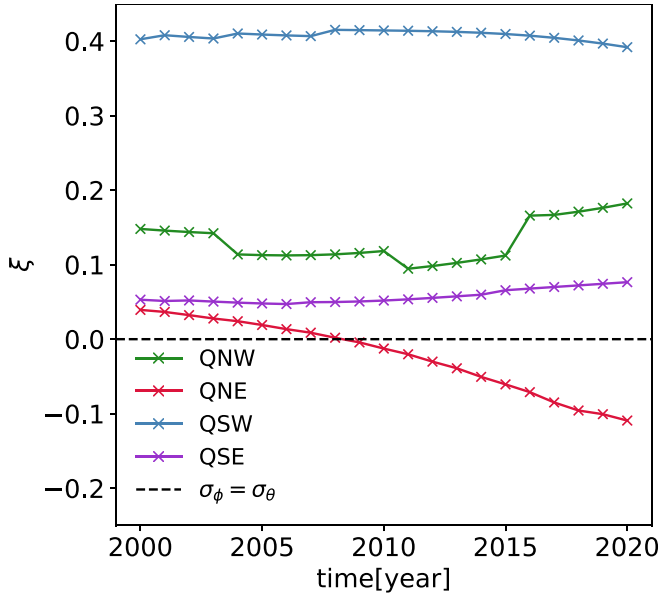

Fig. 12. As in Fig. 10 for the CHAOS7.13 geomagnetic field model.

way to infer stretching effects at the top of Earth's core. Our results may provide valuable constraints on core flow inversions and Earth-like numerical dynamo models.

The core flow that produces, maintains and modifies intense geomagnetic flux patches is complex in space and time. Patches' evolution is subject to contributions from advection, stretching and diffusion as well as the level of alignment of the flow and the field. Our idealized kinematic scenarios are obviously oversimplified, from which we can isolate particular inductive effects and gain fundamental understanding. Upwelling/Downwelling is most efficient in producing changes in patch amplitude and area, whereas horizontal shear flow is most efficient in producing changes in anisotropy of magnetic flux patches. Field-flow alignment strongly affects the time dependence of flux concentration efficiency.

Applied to the historical intense high-latitude geomagnetic flux patches, we find that several early patches match the kinematics of off-phase upwellings. More recent patches showed much more variable kinematics, most notably SV signatures reminiscent of downwellings as well as intermittent effects of downwelling and upwelling. These inferences may provide glimpses into the radial motions at the top of Earth's outer core.

Author agreement

We wish to confirm that there are no known conflicts of interest associated with this publication and there has been no significant financial support for this work that could have influenced its outcome.

We confirm that the manuscript has been read and approved by all named authors and that there are no other persons who satisfied the criteria for authorship but are not listed. We further confirm that the order of authors listed in the manuscript has been approved by all of us. We confirm that we have given due consideration to the protection of intellectual property associated with this work and that there are no impediments to publication, including the timing of publication, with respect to intellectual property. In so doing we confirm that we have followed the regulations of our institutions concerning intellectual property.

We understand that the Corresponding Author is the sole contact for the Editorial process (including Editorial Manager and direct communications with the office). He is responsible for communicating with the other authors about progress, submissions of revisions and final approval of proofs. We confirm that we have provided a current, correct email address which is accessible by the Corresponding Author.

CRediT authorship contribution statement

Filipe Terra-Nova: Conceptualization, Methodology, Software, Data curation, Formal analysis, Writing - original draft, Writing - review & editing. **Ingo Wardinski:** Validation, Visualization, Writing - original draft, Writing - review & editing.

Declaration of Competing Interest

The authors declare the following financial interests/personal relationships which may be considered as potential competing interests:

Terra-Nova, F. reports financial support was provided by French Space Agency.

Data availability

Data will be made available on request.

Acknowledgments

We thank two anonymous reviewers for their constructive comments. F.T.-N. was supported by the Centre national d'études spatiales (CNES).

References

Alken, P., Thébault, E., Beggan, C., et al., 2021. International geomagnetic reference field: the thirteenth generation. Earth Planets Space 49, 73.
Amit, H., 2014. Can downwelling at the top of the Earth's core be detected in the geomagnetic secular variation? Phys. Earth Planet. Inter. 229, 110–121.
Amit, H., Olson, P., 2004. Helical core flow from geomagnetic secular variation. Phys. Earth Planet. Inter. 147, 1–25.
Amit, H., Olson, P., 2006. Time-average and time-dependent parts of core flow. Phys. Earth Planet. Inter. 155, 120–139.
Amit, H., Pais, M.A., 2013. Differences between tangential geostrophy and columnar flow. Geophys. J. Int. 94 (1), 145–157.
Amit, H., Aubert, J., Hulot, G., 2010. Stationary, oscillating or drifting mantle-driven geomagnetic flux patches? J. Geophys. Res. 115, B07108 https://doi.org/10.1029/2009JB006542.
Amit, H., Korte, M., Aubert, J., Constable, C.G., Hulot, G., 2011. The time-dependence of intense archeomagnetic flux patches. J. Geophys. Res. 116, B12106 https://doi.org/10.1029/2011JB008538.
Backus, G.E., 1968. Kinematics of geomagentic secular variation in a perfectly conducting core. Philos. Trans. R. Soc. Lond. A263, 239–266.
Baerenzung, J., Holschneider, M., Lesur, V., 2016. The flow at the Earth's core-mantle boundary under weak prior constraints. J. Geophys. Res. Solid Earth 121, 1343–1364.
Baerenzung, J., Holschneider, M., Wicht, J., Sanchez, S., Lesur, V., 2018. Modeling and predicting the short-term evolution of the geomagnetic field. J. Geophys. Res. Solid Earth 123, 4539–4560.
Barrois, O., Gillet, N., Aubert, J., 2017. Contributions to the geomagnetic secular variation from a reanalysis of core surface dynamics. Geophys. J. Int. 211 (1), 50–68.
Bloxham, J., 1986. The expulsion of magnetic flux from the Earth's core. Geophys. J. R. Astron. Soc. 87, 669–678.
Bloxham, J., 1992. The steady part of the secular variation of the Earth's magnetic field. J. Geophys. Res. 97, 19565–19579.
Bloxham, J., Jackson, A., 1991. Fluid flow near the surface of the Earth's outer core. Rev. Geophys. 29, 97–120.
Cao, H., Yadav, R.K., Aurnou, J.M., 2018. Geomagnetic polar minima do not arise from steady meridional circulation. Proc. Natl. Acad. Sci. 115, 11186–11191.
Christensen, U.R., Olson, P., Glatzmaier, G., 1998. A dynamo model interpretation of geomagnetic field structures. Geophys. Res. Lett. 25, 1565–1568.
Chulliat, A., Hulot, G., Newitt, L.R., 2010. Magnetic flux expulsion from the core as a possible cause of the unusually large acceleration of the north magnetic pole during the 1990s. J. Geophys. Res. 115, B07101 https://doi.org/10.1029/2009JB007143.
Constable, C., 2007. Non-dipole field. In: Gubbins, D., Herrero-Bervera, E. (Eds.), Encyclopedia of Geomagnetism and Paleomagnetism. Springer, Dordrecht, pp. 701–704.
Courant, R., Friedrichs, K., Lewy, H., 1928. Über die partiellen Differenzengleichungen der mathematischen Physik. Math. Ann. 100, 32–74.
Dumberry, M., Finlay, C.C., 2007. Eastward and westward drift of the Earth's magnetic field for the last three millennia. Earth Planet. Sci. Lett. 254, 146–157.
Eymin, C., Hulot, G., 2005. On surface core flows inferred from satellite magnetic data. Phys. Earth Planet. Inter. 152, 200–220.
Finlay, C.C., Amit, H., 2011. On flow magnitude and field-flow alignment at Earth's core surface. Geophys. J. Int. 186, 175–192.
Finlay, C., Kloss, C., Olsen, N., et al., 2020. The CHAOS-7 geomagnetic field model and observed changes in the South Atlantic anomaly. Earth Planets Space 72, 156.
Friis-Christensen, E., Lühr, H., Hulot, G., 2006. Swarm: a constellation to study the Earth's magnetic field. Earth Planets Space 58, 351–358.
Gillet, N., Pais, M.A., Jault, D., 2009. Ensemble inversion of time-dependent core flow models. Geochem. Geophys. Geosyst. 10, Q06004.
Gillet, N., Barrois, O., Finlay, C.C., 2015. Stochastic modelling of the earth's magnetic field: inversion for covariances over the observatory era. Earth Planets Space 67, 67–71.
Gillet, N., Huder, L., Aubert, J., 2019. A reduced stochastic model of core surface dynamics based on geodynamo simulations. Geophys. J. Int. 219 (1), 539–552.
Gubbins, D., 2003. Thermal core-mantle interactions: theory and observations. In: Dehant, V., Creager, K., Karato, S., Zatman, S. (Eds.), *Earth's Core: Dynamics, Structure And Rotation*, AGU Geodynamics Series - American Geophysical Union.
Gubbins, D., Davies, C.J., 2013. The stratified layer at the core-mantle boundary caused by barodiffusion of oxygen, Sulphur and silicon. Phys. Earth Planet. Inter. 215, 21–28.
Gubbins, D., Willis, A.P., Sreenivasan, B., 2007. Correlation of Earth's magnetic field with lower mantle thermal and seismic structure. Phys. Earth Planet. Inter. 162, 256–260.
Helffrich, G., Kaneshima, S., 2010. Outer-core compositional stratification from observed core wave speed profiles. Nature 468, 807–810.
Holme, R., 2015. Large-scale flow in the core. In: Schubert, G. (Ed.), Treatise on Geophysics, second edition. Elsevier.
Huguet, L., Amit, H., Alboussière, T., 2018. Geomagnetic dipole changes and upwelling/downwelling at the top of the Earth's core. Front. Earth Sci. 6, 170.
Irving, J., Cottaar, S., Lekić, V., 2018. Seismically determined elastic parameters for Earth's outer core. Sci. Adv. 4 (6) eaar2538.
Jackson, A., 2003. Intense equatorial flux spots on the surface of the Earth's core. Nature 424, 760–763.
Jackson, A., Jonkers, A.R.T., Walker, M.R., 2000. Four centuries of geomagnetic secular variation from historical records. Philos. Trans. R. Soc. Lond. A358, 957–990.
Jaqueto, P., Trindade, R., Terra-Nova, F., et al., 2022. Stalagmite paleomagnetic record of a quiet mid-to-late Holocene field activity in Central South America. Nat. Commun. 13, 1349.
Jonkers, A.R.T., Jackson, A., Murray, A., 2003. Four centuries of geomagnetic data from historical records. Rev. Geophys. 41 https://doi.org/10.1029/2002RG000115.
Kac, M., 1939. On a characterization of the normal distribution. Am. J. Math. 61, 726–728.
Kelly, P., Gubbins, D., 1997. The geomagnetic field over the past 5 million years. Geophys. J. Int. 128, 315–330.
Konôpková, Z., McWilliams, R., Gómez-Pérez, N., Goncharov, A.F., 2016. Direct measurement of thermal conductivity in solid iron at planetary core conditions. Nature 534, 99–101.
LeMouël, J.L., 1984. Outer core geostrophic flow and secular variation of Earth's magnetic field. Nature 311, 734–735.
Lesur, V., Whaler, K., Wardinski, I., 2015. Are geomagnetic data consistent with stably stratified flow at the core–mantle boundary? Geophys. J. Int. 201 (2), 929–946.
Lézin, M., Amit, H., Terra-Nova, F., Wardinski, I., 2023. Mantle-driven north-south dichotomy in geomagnetic polar minima. Phys. Earth Planet. Inter. 337, 107000.
Livermore, P., Hollerbach, R., Finlay, C., 2017. An accelerating high-latitude jet in Earth's core. Nat. Geosci. 10, 62–68.
Masters, G., Laske, G., Bolton, H., Dziewonski, A., 2000. The relative behavior of shear velocity, bulk sound velocity, and compressional velocity in the mantle: implications for chemical and thermal structure. In: Karato, S., Forte, A., Liebermann, R., Masters, G., Stixrude, L. (Eds.), Earth's Deep Interior: Mineral Physics and Tomography from the Atomic to the Global Scale. AGU monograph, Washington D. C.
Matzka, J., Chulliat, A., Mandea, M., Finlay, C.C., Qamili, E., 2010. Geomagnetic observations for main field studies: from ground to space. Space Sci. Rev. 155, 29–64.
Metman, M.C., Livermore, P.W., Mound, J.E., 2018. The reversed and normal flux contributions to axial dipole decay for 1880–2015. Phys. Earth Planet. Inter. 276, 106–117.
Mound, J., Davies, C., Rost, S., Aurnou, J., 2019. Regional stratification at the top of earth's core due to core–mantle boundary heat flux variations. Nat. Geosci. 12, 575–580.
Olson, P., Aurnou, J., 1999. A polar vortex in the Earth's core. Nature 402, 170–173.
Olson, P., Christensen, U.R., 2002. The time averaged magnetic field in numerical dynamos with nonuniform boundary heat flow. Geophys. J. Int. 151, 809–823.
Olson, P., Christensen, U.R., Glatzmaier, G.A., 1999. Numerical modeling of the geodynamo: mechanisms of field generation and equilibration. J. Geophys. Res. 104, 10383–110404.
Olson, P., Landeau, M., Reynolds, E., 2017. Dynamo tests for stratification below the core-mantle boundary. Phys. Earth Planet. Inter. 271, 1–18.
Pais, M.A., Jault, D., 2008. Quasi-geostrophic flows responsible for the secular variation of the Earth's magnetic field. Geophys. J. Int. https://doi.org/10.1111/j.1365–246X.2008.03741.x.

Pinheiro, K.J., Amit, H., Terra-Nova, F., 2019. Geomagnetic jerk features produced using synthetic core flow models. Phys. Earth Planet. Inter. 291, 35–53.
Pozzo, M., Davies, C., Gubbins, D., Alfè, D., 2012. Thermal and electrical conductivity of iron at Earth's core conditions. Nature 485, 355–358.
Rau, S., Christensen, U.R., Jackson, A., Wicht, J., 2000. Core flow inversion tested with numerical dynamo models. Geophys. J. Int. 141, 485–497.
Roberts, P.H., 2007. Theory of the geodynamo. In: Olson, P. (Ed.), Treatise on Geophysics. Elsevier.
Roberts, P.H., Scott, S., 1965. On analysis of the secular variation, 1, a hydromagnetic constraint: theory. J. Geomagn. Geoelectr. 17, 137–151.
Terra-Nova, F., Amit, H., 2020. Magnetic boundary layers in numerical dynamos with heterogeneous outer boundary heat flux. Phys. Earth Planet. Inter. 309, 106589.
Terra-Nova, F., Amit, H., Hartmann, G.A., Trindade, R.I.F., 2015. The time dependence of reversed archeomagnetic flux patches. J. Geophys. Res. 120 (2), 691–704.
Terra-Nova, F., Amit, H., Choblet, G., 2019. Preferred locations of weak surface field in numerical dynamos with heterogeneous core-mantle boundary heat flux: consequences for the South Atlantic anomaly. Geophys. J. Int. 217 (2), 1179–1199.
Troyano, M., Fournier, A., Gallet, Y., Finlay, C., 2020. Imprint of magnetic flux expulsion at the core–mantle boundary on geomagnetic field intensity variations. Geophys. J. Int. 221 (3), 1984–2009.
Whaler, K., 1980. Does the whole of Earth's core convect? Nature 287, 528–530.